coatings

MDPI

Article

Structure and Void Connectivity in Nanocolumnar Thin Films Grown by Magnetron Sputtering at Oblique Angles

Rafael Alvarez [1,2,*], Guillermo Regodon [1], Hiedra Acosta-Rivera [1], Victor Rico [1], German Alcala [3], Agustín R. González-Elipe [1] and Alberto Palmero [1,*]

[1] Instituto de Ciencia de Materiales de Sevilla, CSIC—Universidad de Sevilla, Américo Vespucio 49, 41092 Seville, Spain
[2] Departamento de Física Aplicada I, Escuela Politécnica Superior, Universidad de Sevilla, c/Virgen de África 7, 41011 Seville, Spain
[3] Departamento de Ingeniería Química y Materiales, Facultad de Ciencias Químicas, Universidad Complutense de Madrid, Avenida Complutense s/n, 28040 Madrid, Spain
* Correspondence: ralvarezmol@us.es (R.A.); alberto.palmero@csic.es (A.P.)

Abstract: The morphology and void connectivity of thin films grown by a magnetron sputtering deposition technique at oblique geometries were studied in this paper. A well-tested thin film growth model was employed to assess the features of these layers along with experimental data taken from the literature. A strong variation in the film morphology and pore topology was found as a function of the growth conditions, which have been linked to the different collisional transport of sputtered species in the plasma gas. Four different characteristic film morphologies were identified, such as (i) highly dense and compact, (ii) compact with large, tilted mesopores, (iii) nanocolumns separated by large mesopores, and (iv) vertically aligned sponge-like coalescent nanostructures. Attending to the topology and connectivity of the voids in the film, the nanocolumnar morphology was shown to present a high pore volume and area connected with the outside by means of mesopores, with a diameter above 2 nm, while the sponge-like nanostructure presented a high pore volume and area, as well as a dense network connectivity by means of micropores, with a diameter below 2 nm. The obtained results describe the different features of the porous network in these films and explain the different performances as gas or liquid sensors in electrochromic applications or for infiltration with nanoparticles or large molecules.

Keywords: magnetron sputtering; oblique angle deposition; nanocolumnar thin films; porous coatings; physical vapor deposition

Citation: Alvarez, R.; Regodon, G.; Acosta-Rivera, H.; Rico, V.; Alcala, G.; González-Elipe, A.R.; Palmero, A. Structure and Void Connectivity in Nanocolumnar Thin Films Grown by Magnetron Sputtering at Oblique Angles. *Coatings* **2023**, *13*, 991. https://doi.org/10.3390/coatings13060991

Academic Editor: Frederic Sanchette

Received: 4 May 2023
Revised: 19 May 2023
Accepted: 23 May 2023
Published: 26 May 2023

1. Introduction

The last years have witnessed the flourishing of numerous applications and technological devices based on nanocolumnar porous, thin films [1]. These are formed by nanocolumns with a typical diameter and side-to-side distance in the order of 100 nm, making these materials less dense and with a much larger specific surface than their compact counterpart [2–4], and with different optical, electrical, and magnetic properties [5–12]. These features make them good candidates for the development of numerous technological devices, such as gas or liquid sensors, optical coatings, and electrodes or instruments for fluid manipulation, among others [13–26]. They are also applied in biomedicine, as the surface energy of the film and its interaction with living organisms can be tuned by modifying the features of the columnar arrangement [27,28]. In all these cases, and aside from the chemical composition of the film, a key feature defining their functionality resides in the characteristics of the porous structure. As a matter of fact, the nanocolumns are far from being smooth and compact, but are rather rough and with numerous highly connected cavities that penetrate deeply into the film, thus increasing the overall film surface [29,30]. However, not all these pore cavities are fully accessible when these films are put into contact

with air or an external fluid, as they might be connected by very narrow throats which may preclude a smooth diffusion mechanism [31–33].

In general, the nanocolumnar structures emerge during growth thanks to a certain geometrical arrangement of the deposition setup, the so-called glancing or oblique angle configuration [1,34]. This arrangement promotes the deposition on a substrate of species directed along a well-defined oblique direction, which causes the appearance of surface shadowing mechanisms, the formation of a few nanometers-thick continuous layers on the substrate and, eventually, the development of nanocolumnar structures [35]. Classically, this type of morphology has been obtained using the evaporation technique [36,37] at glancing angles, by which a given material is sublimated in a vacuum reactor, forming a gaseous flux of species that are deposited on a substrate situated off-axis [38]. Yet, the difficulty to upscale this arrangement to operate over large surfaces, a key feature to implement the technique for industrial applications, has motivated the adoption of more sophisticated approaches, such as the magnetron sputtering technique using oblique angle deposition (MS-OAD), which is a variation of the classical magnetron sputtering technique [1]. In this case, an argon plasma is made to interact with a solid plate, the target, causing the sputtering of species from it, preferentially in the direction perpendicular to the target surface [39,40]. In this way, the oblique angle configuration is usually achieved by placing a substrate in front of the target and tilting it an angle α with respect to the surface of the target, although other operational geometries have also been proposed in the last years, targeting specific industrial applications [27,41].

The morphology of thin films grown by MS-OAD shows a strong dependence on two key experimentally controllable quantities: the pressure of the gases in the deposition reactor, p_g, and the tilt angle of the substrate, α. In this way, p_g determines the mean free path of the sputtered species in the plasma, and thus their collisional transport from the target towards the substrate [42]. For instance, in the limit of very high pressures (typically well above 1 Pa), the movement of sputtered species in the plasma gas becomes randomized due to the large number of collisions previous to their deposition, so they may arrive at the substrate following a Brownian-like trajectory and an isotropic momentum distribution, thus precluding the formation of nanocolumns [43]. Under these conditions, the film morphology is known to contain numerous vertically aligned and coalescent sponge-like structures [42], which from now forth will be simply dubbed sponge-like morphology in this paper. On the other hand, in the low-pressure limit, most sputtered particles do not experience collisions in the plasma and arrive at the substrate with the kinetic energy and direction of movement with which they leave the target, along a so-called ballistic trajectory [44]. Under these last conditions, in Ref. [42] it was experimentally demonstrated that the morphology of Au thin films grown by MS-OAD strongly depended on α, yielding typical compact structures when α was below 45°, as well as compact structures containing large and tilted embedded pores for increasing values of α up to ~70°. Moreover, when α was above ~70°, well-separated and tilted nanocolumnar structures were reported.

Much research has been carried out in the last years in order to characterize the porous network in the films in terms of morphology and connectivity. With respect to classical gas adsorption methods widely used to characterize powder materials [45], a clear shortcoming of the characterization of thin film porosity is the relatively low amount of material available, which generally precludes the use of classical BET adsorption methods using N_2 as the adsorbing gas. Nevertheless, in Ref. [32], the pore size distribution in evaporated nanocolumnar TiO_2 and SiO_2 thin films was studied, circumventing this limitation by analyzing the adsorption isotherm curves with Kr gas, finding out that the size of the pores was maximized for the film grown with an angle of incidence of $\sim 70°$ for TiO_2. Likewise, in Ref. [31], a similar adsorption approach was adopted, using water as the adsorbing gas and measuring the adsorption isotherm with a quartz crystal monitor. This time, it was found that the pore volume accessible to water condensation could spread up to 60% of the total film volume. Adsorption isotherms of different vapors in porous optical multilayers

have also been obtained using optical methods [46,47]. Moreover, in Ref. [3], the efficiency of porous WO_3 thin films prepared by MS-OAD as cathodes for electrochromic applications was analyzed when they were put into contact with a liquid electrolyte. There, it was found that the total void space in the film was not the relevant quantity defining the electrochromic efficiency, but rather the so-called accessible volume and the actual contact area, defined, respectively, as the volume inside the film that is actually filled by the electrolyte and its surface. Remarkably, it was found that the sponge-like morphology presented better electrochromic efficiency than a nanocolumnar film when used as a cathode, despite both having similar total void volumes, which was a clear indication of the relevance of the void connectivity for this particular application. This analysis has motivated this paper, where a well-tested model of the film growth is used to systematically analyze the influence of p_g and α on the pore features, as well as analyze the main differences between sponge-like and nanocolumnar film morphologies in terms of porosity. As a case example, the focus has been set on a particular material such as TiO_2 grown by MS-OAD due to the multiple technological applications it presents, although the results and discussion can be easily extrapolated to other materials and conditions.

2. Growth Model and Pore Analysis

2.1. Growth Simulation

The growth model has been explained in detail in Ref. [48], where it was proven adequate to describe the morphological features of different thin films by MS-OAD at low temperatures. Next, we briefly present its basics, although, for additional information, it is advised to check Ref. [48]. Sputtered Ti species are considered to leave the racetrack of the target with a momentum distribution $F\left(\vec{p}\right)$, calculated by the software SRIM (James F. Ziegler, Annapolis, MD, USA) (version 2013) [49], where $\vec{p}$ is the linear momentum. Along their way to the substrate, they experience scattering events with the plasma-heavy species until they are deposited, arriving with a momentum distribution function $f\left(\vec{p}\right)$, which can be calculated by the software SIMTRA (Ghent University, Ghent, Belgium) (version 2.2) [50,51]. The incorporation of these species to the growing film is simulated by using a home-made MatLab code and Monte Carlo techniques; the space over the substrate is divided into a $N_L \times N_L \times N_H$ 3D array (N_L is the number of cells along the two Cartesian axes parallel to the substrate, while N_H represents the number of cells along the Cartesian axis perpendicular to the substrate), where each cell has the value 1 if it contains a deposited species and 0 otherwise. In this way, the deposition atoms move towards the substrate from a random initial location above the film surface, following a straight trajectory defined by $\vec{p}$, which is randomly obtained from $f\left(\vec{p}\right)$. The movement continues in the 3D grid, using periodic boundary conditions, until the species arrive at the substrate or attempt to move into an occupied cell, where different mobility processes are induced depending on its kinetic energy, as described in Ref. [52] (see also Ref. [48] for more details).

After the incorporation of a sputtered Ti species into the film, it is considered that the continuous impingement of oxygen species on the growing film surface causes its oxidation, becoming TiO_2. Consequently, the volume of each cell in the cubic array can be estimated by the volume of a TiO_2 species in the film, which attending to the typical density of TiO_2, yields a length of the cell edge of ~ 0.4 nm. Here, it is important to underline that no thermally induced mobility processes are introduced in the model, implying that the calculated results will only be valid when the growth takes place in Zone I of the Thornton Structure Zone Model [53,54]. The working pressure was varied in each simulation from 0.2 to 2 Pa, and the value of α from 0° to 180°.

2.2. Simulation Conditions

The simulation conditions aim at reproducing the experimental setup presented in Refs. [41,55], where the experimental details are given. Yet, for the sake of clarity, in Figure 1 the main geometrical details of the simulation conditions are presented: a 3-inches diameter

Ti target was considered, located $L = 7$ cm apart from a rotatable substrate holder. An Ar pressure ranging from 0.20 to 1 Pa was considered, while the oxygen partial pressure was set to 0.05 Pa. A DC target voltage of ~ 300 V was considered in all the cases. Given the circular shape of the target, the substrate rotation angle, α, and the ballistic angle of incidence, α_i, are related by means of the linear relation $\alpha_i = \alpha - \Delta$, with $\Delta = tan^{-1}(R/L)$, being $R = 2$ cm the radius of the racetrack (the circular region of the target where species are sputtered from), and consequently $\Delta \sim 15°$ (see Figure 1).

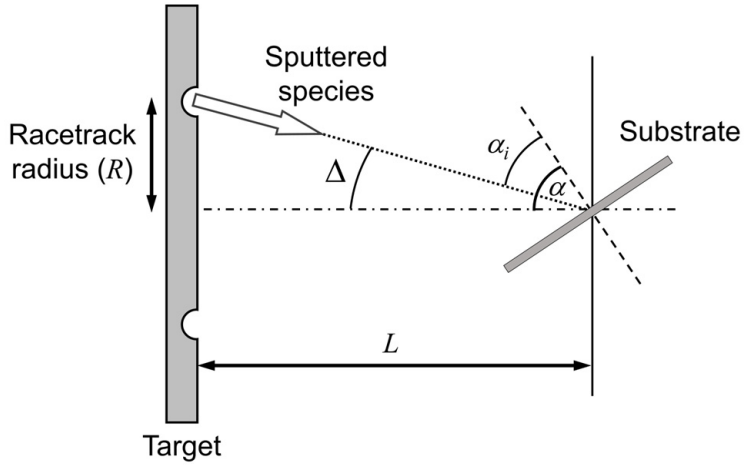

Figure 1. Scheme of the simulated experimental setup and the difference between the angle of incidence, α_i, and the substrate rotation angle, α.

The simulated films have been compared with experimental data taken from Refs. [41,55]. All these films had a composition of TiO_2, being transparent in the visible range of the spectrum [56]. In Ref. [55] the aim was to compare the nanocolumnar growth of TiO_2 thin films when using either a pure DC or a pulsed DC electromagnetic signal to maintain the plasma discharge. For this paper, only the films grown with a DC signal are considered. The films were grown for different values of the substrate rotation angle, $\alpha = 60°, 70°, 80°$, and 85° which resulted in an angle of incidence of $\alpha_i = 45°, 55°, 65°$, and 70°. The density of these films was measured by means of Rutherford Backscattering Spectroscopy (RBS), and it was employed to assess the total void space in the films, just by comparing the obtained value of the film density with that of a fully compact film. In Ref. [41], the same setup described above to grow TiO_2 thin films was employed, this time setting the substrate rotation angle at $\alpha = 95°$ (or likewise $\alpha_i = 80°$) and the total deposition pressure at three different values, $p_g = 0.2$–0.3, 0.5–0.6, and 0.8–0.9 Pa. In that work, films grown with and without the presence of a collimator were compared. For this work only the cases grown in standard conditions (in absence of a collimator) were analyzed. All these films were transparent in the visible part of the spectrum, indicating that its composition was TiO_2 [56]. This result was also corroborated by analyzing the proportion O:Ti in the films as obtained by the RBS measurements.

2.3. Pore Network Characterization

The void space structure of the simulated films was characterized using the same concepts defined in Ref. [29]. The parameter ϕ, dubbed the pore throat, is introduced to topologically characterize the void space, as follows: two voids in the film are considered connected and, thus, to belong to the same pore if a sphere of diameter ϕ may follow a continuous path from one to the other through void space, not touching any material (see Figure 2a for a scheme). If this path does not exist, both voids are considered not connected, and, hence, to belong to different and independent pores. Following this idea, three relevant quantities that will be studied in detail in this paper are defined:

- The void space, v_T, defined as the total volume inside the film not occupied by material (see Figure 2b for a scheme). This quantity, therefore, does not consider any type of connectivity, and can be calculated by means of the film density, ρ, through the formula $v_T = 1 - \rho/\rho_c$, where ρ_c is the density of a fully compact film.
- The void volume connected with the outside, v_ϕ, (see Figure 2b for a scheme) defined as the volume of the voids within the film that are connected with the outside by means of a pore throat ϕ. Therefore, according to the definition of connectivity made above, a sphere with a diameter ϕ may follow a continuous path from any point within this volume to the exterior of the film, not touching any material.
- The contact area of the void volume connected with the outside, a_ϕ (see Figure 2b for a scheme), as the area corresponding to v_ϕ.

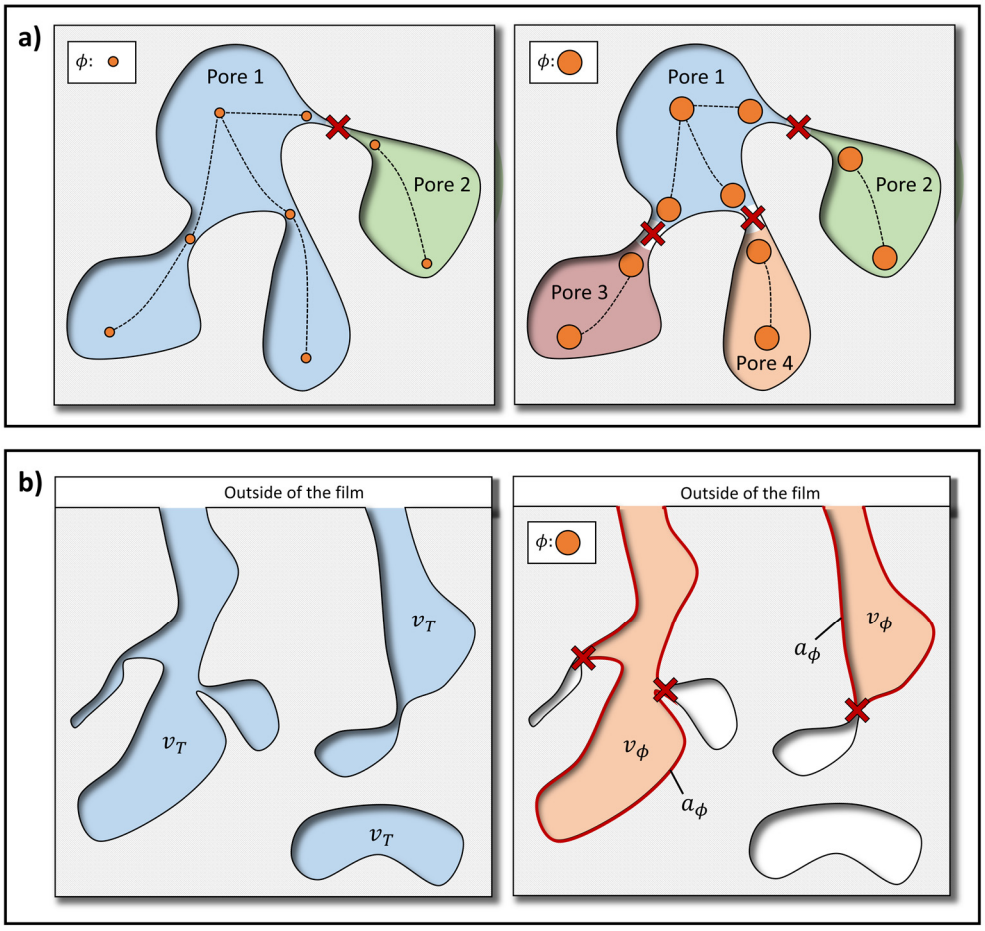

Figure 2. Illustration of the concept of pore throat, ϕ: (**a**) two voids within the film are considered connected if a sphere with diameter ϕ may continuously move from one void to the other without intercepting any material and (**b**) illustration of the concept of total void volume (v_T), and volume (v_ϕ) and area (a_ϕ) of the voids connected with the outside of the film.

3. Results and Discussion

3.1. Morphology of the Films

In Figure 3 we show the cross-sectional images of a set of simulations performed at a relatively low deposition pressure, $p_g = 0.2$ Pa, and for increasing values of α. There, we notice the progressive structural shift of the films, from a compact morphology when $\alpha \lesssim 60°$, to a morphology defined by tilted pores that extend from the very surface of the film to the bottom for $60° \lesssim \alpha \lesssim 85°$. Moreover, the nanocolumnar morphology emerges when $\alpha \gtrsim 85°$. These generic morphologies are in agreement with other results from the literature for Au thin films grown by MS-OAD at relatively low pressures [42], by

considering that $\alpha_i = \alpha - \Delta$, with $\Delta \sim 15^\circ$ in our case. Remarkably, Figure 3 indicates an additional phenomenon that, to our knowledge, has not been yet reported in the literature: when $\alpha \gtrsim 100^\circ$ the columns start to straighten up. Outstandingly, this trend is similar to that found when increasing the deposition pressure, which is presented in Figure 4. There, the effect of increasing p_g from 0.2 to 1 Pa when $\alpha = 100^\circ$ is depicted, and it is clear that the nanocolumns progressively straighten up as well, until becoming completely vertical at very high pressures. This latter trend was already explained in Ref. [42] and is associated with an increasing amount of Brownian-like deposition species in the plasma due to the shorter mean free path of these species with increasing pressures, in detriment of well-directed ballistic species. For comparison purposes, in Figure 4 an image of the limit case when all sputtered species arrive at the film from any random direction (i.e., all deposition species are Brownian-like) is included. This case depicts a structure similar to the $p_g = 1$ Pa case in Figure 4 and the $\alpha = 180^\circ$ case in Figure 3, implying that the film nanostructure in these two cases corresponds to the sponge-like morphology, as commented in the introduction section. Yet, the appearance of this same morphology at low pressures in Figure 3, as well as the straightening up of the nanocolumns when $\alpha > 100^\circ$ (i.e., $\alpha_i = 85^\circ$), must have another origin, since the mean free path of sputtered species does not depend on α and, at relatively low pressures, the transport is dominated by ballistic species.

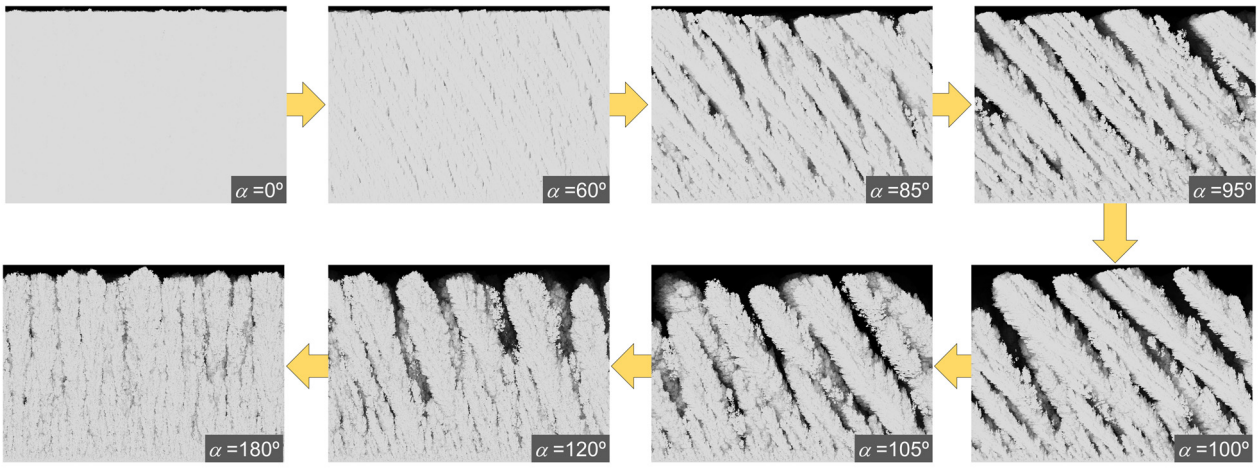

Figure 3. Cross-sectional images of the simulated films, when $p_g = 0.2$ Pa, for different values of α. Film thickness is 250 nm.

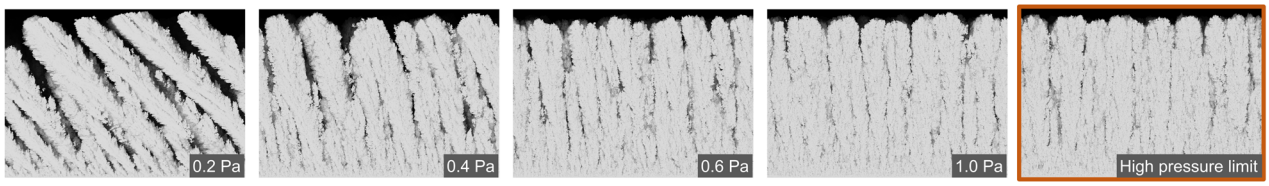

Figure 4. Cross-sectional images of the simulated films when increasing p_g up to 1 Pa when $\alpha = 100^\circ$. As a Reference, the simulated film nanostructure in the high-pressure limit is also included. Film thickness is 250 nm.

In order to analyze the appearance of the sponge-like morphology as a limit case in Figure 3, the software SIMTRA (Ghent University, Ghent, Belgium) (version 2.2) [50,51] has been used to calculate the function $f(\theta)$, defined as the distribution function of possible angles of incidence of sputtered species arriving at the substrate, where θ represents this angle of incidence as measured from the substrate normal. This function is depicted in Figure 5 for different values of α and for $p_g = 0.2$ Pa, normalized to the total number of sputtered atoms. Furthermore, $f(\theta)$ has been separated in two components according to the

energy of the arriving species, where the threshold corresponds to the energy of a particle following a thermal motion defined by the temperature of the argon neutral atoms, T_g. Since T_g is below 600 K under typical magnetron sputtering conditions, the typical kinetic energy of Brownian-like species is below $3k_BT_g/2$ ~0.05 eV. Figure 5a shows $f(\theta)$ for the species with kinetic energies above 0.05 eV, which correspond to those species that still keep part of the original energy and momentum when sputtered, i.e., ballistic species (and those in an intermediate state). Figure 5b shows $f(\theta)$ for those with kinetic energies in the thermal range below 0.05 eV, i.e., those that follow a Brownian-like trajectory. For $\alpha = 60°$, Figure 5a indicates the existence of a clear ballistic peak at $\alpha_i \sim 45°$, corroborating that $\Delta \sim 15°$ in our conditions. Moreover, when α increases, a shift of the ballistic peak towards higher angles of incidence becomes evident, along with a remarkable decrease in the height of the peak. This phenomenon is related to the area (cosine) factor modulating the arrival rate of these well-directed species when tilting the substrate. However, the angular distribution of Brownian-like species in Figure 5b is not only independent of the particular value of α, which is coherent with their isotropic momentum distribution in the plasma phase, but it also depicts a shape $\sim sin\theta cos\theta d\theta$ (also included in Figure 5b), which is well known for describing the deposition flux of species with an isotropic momentum distribution in a plasma gas [57]. Therefore, it is obtained that, for a given pressure, there is a constant number of Brownian-like species that act as background contribution to the film growth no matter the value of α, while the ballistic contribution diminishes with α. Consequently, there is a critical angle, $\alpha = \alpha_M$, above which the ballistic component is small enough to allow Brownian-like species to start affecting the nanocolumnar growth, which results in the progressive straightening up of the nanocolumns. In this way, the condition $\alpha = \alpha_M$ would yield the film containing better defined and well-separated nanocolumns with a maximum tilt angle, which according to Figure 3 results in $\alpha_M \sim 100°$ (corresponding to an angle of incidence of $\alpha_i \sim 85°$) when $p_g = 0.2$ Pa. Moreover, as α increases, the deposition of ballistic species as well as those in an intermediate state decrease, finding in the limit case of $\alpha = 180°$ that the growth is only carried out by Brownian-like species. Thus, under those conditions, a sponge-like morphology is grown, equal to that obtained at high pressures. This is clearly visible in Figure 6, where the calculated value of the tilt angle of the nanocolumns with respect to the substrate normal, β, is displayed as a function of α for different values of p_g, and where β is found to increase up to a certain angle of incidence, $\alpha = \alpha_M$, above which β decreases down to 0°, in agreement with the progressive straightening up of the nanocolumns. Remarkably, an increase of p_g in Figure 6 does not only cause the progressive flattening of the curve but also a shift in α_M towards lower values. This trend is explained by the overall increase in Brownian-like species with the pressure in detriment of ballistic ones, thus the straightening up process will start at lower values of α.

Furthermore, the discussion above also explains why this characteristic phenomenon was not previously detected for Au thin films in Ref. [42], as the large atomic mass of Au in comparison with Ti makes more difficult the complete loss of original kinetic energy and momentum (i.e., Au sputter atoms would require more collisions than Ti atoms to become Brownian-like). Therefore, under the same pressure conditions, the Au deposition flux would contain less Brownian-like species than in the case of Ti, making the value of α_M to be above the studied range in Ref. [42]. In order to check experimental evidence on these results, experimental data obtained at $p_g = 0.2$–0.3 Pa as a function of α have been included in Figure 6, taken from Refs. [41,55], where an experimental setup similar to the one considered in this article (see Figure 1) was employed. In this way, the good agreement between the experimental values and the presented model can be appreciated, as well as the existence of α_M when operating at relatively low pressures and high angles of incidence.

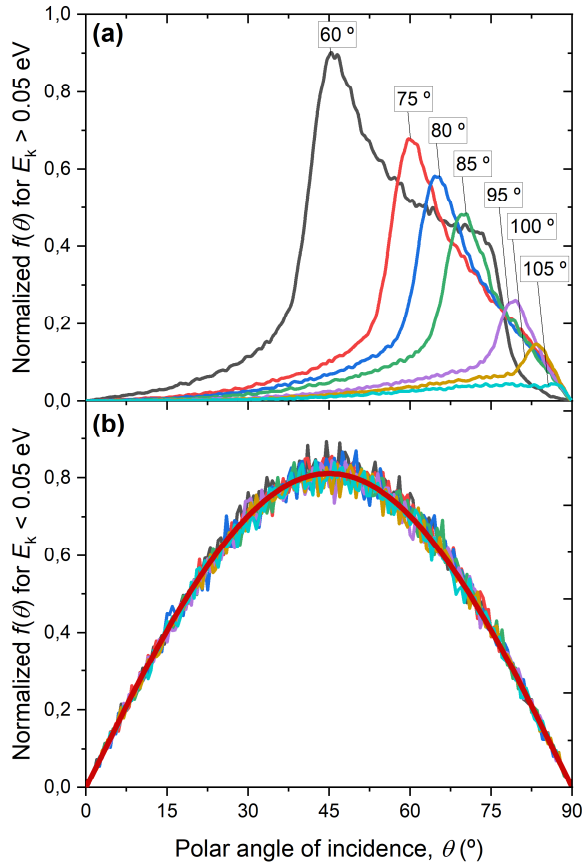

Figure 5. Calculated incident polar angle distribution function of the deposition species on the substrate for a pressure $p_g = 0.2$ Pa and for different values of α, normalized to the number of sputtered particles. (**a**) Distribution function of the species with kinetic energy above 0.05 eV and (**b**) distribution function of the species with kinetic energy below 0.05 eV. In (**b**) the typical shape of the distribution function corresponding to a deposition flux of species with isotropic momentum distribution in the gas phase ($\sim sin\theta cos\theta d\theta$) is included.

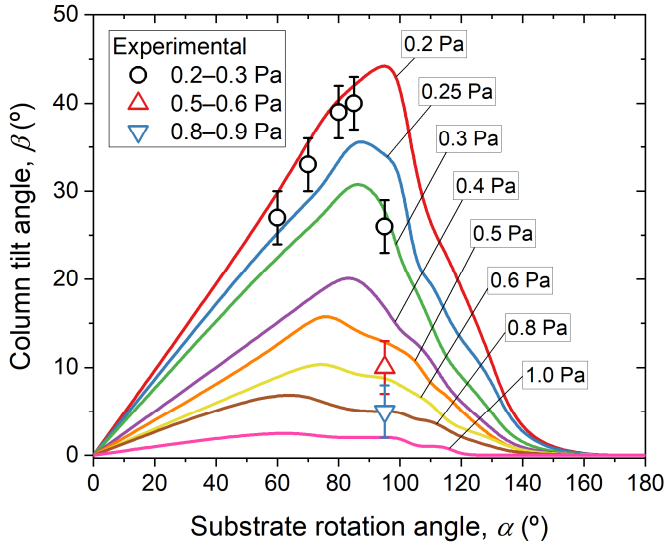

Figure 6. Calculated values of the column tilt angle, β, as a function of the substrate rotation angle, α, and pressure, p_g, in the deposition reactor. Experimental data taken from Refs. [41,55] have been included.

3.2. Topology of the Porous Structure in Contact with the Outside

In Figure 7, the proportion of void space in the films, v_T, as a function of α is shown for different values of p_g. For a pressure of 0.2 Pa, four different regions are again distinguished for increasing values of α, in agreement with the discussion above on film morphology. When $\alpha < 60°$ (when the structure is compact, according to Figure 3) a linear increase of v_T is obtained. Moreover, when $60° \lesssim \alpha \lesssim 85°$ the curve bends upwards, corresponding to the appearance of the tilted mesopores, while for $85° \lesssim \alpha \lesssim \alpha_M$ a rather linear trend is again found, with a higher slope than the previous one, corresponding to the region where the nanocolumns develop. Finally, when $\alpha > \alpha_M$, the curve flattens and stays at a constant value of $v_T \sim 65\%$; this means that a nanocolumnar film grown when $\alpha = \alpha_M$ and the sponge-like morphology found when $\alpha = 180°$ (or in the high-pressure limit) remarkably possess a similar amount of void space. For increasing pressures, the same trend is found: all the curves converge to the same value ($v_T \sim 65\%$) whenever the threshold $\alpha = \alpha_M$ is surpassed. In order to better appreciate these changes in the behavior of v_T as a function of α, a differential form of Figure 7 has been included as Supporting Information (Figure S1). For comparison purposes, we have included some experimental data in Figure 7 taken from Ref. [41], for $p_g = 0.2$ Pa and $\alpha = 60°, 70°, 80°$, and 85°, obtained under similar conditions as those depicted in Figure 1, finding again an overall good comparison with the calculated results (note that the case $\alpha = 60°$ corresponds to a sharp transition from a fully compact film to a compact film with tilted mesopores according to Figure 3, which represents an important source of error in this case when comparing with experimental data).

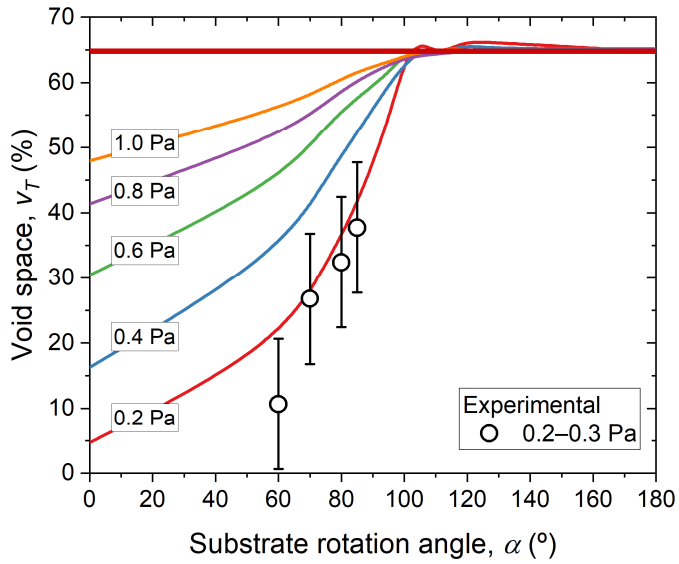

Figure 7. Proportion of void space in the films, v_T, as a function of the substrate rotation angle, α, for different values of the deposition pressure, p_g. Experimental data taken from Ref. [55] have been included. The thick horizontal red line corresponds to the value obtained for the film grown in the high-pressure limit.

At this point, it is important to underline that the quantity v_T analyzed above takes into account all void spaces in the film and, consequently, it contains no information on the void connectivity. In order to study this, the quantity v_ϕ has been introduced as the volume of the voids inside the film connected with the outside by means of a pore throat ϕ (for simplicity reasons, the values of ϕ have been expressed in terms of cells in the model, knowing that the width of a cell is ~0.4 nm). For instance, when $\phi = 5$ (i.e., 2 nm), v_ϕ Refers to all the empty volume inside the film that is connected with the outside by means of a sphere with a diameter of 5 cells; i.e., the connectivity with the outside of the film would only be stablished by means of mesopores (we use here the nomenclature defined by the IUPAC for pores with a diameter above 2 nm [58]), while the remaining void space would

be considered not connected with the outside. On the other hand, when $\phi = 1$ (i.e., 0.4 nm) the connectivity will be higher, since it will be established by micropores (again we use the same nomenclature defined by the IUPAC for pores with a diameter below 2 nm [58]). For illustration purposes, in Figure 8, we have displayed the zoomed view of a nanocolumn (top row) and of a sponge-like (bottom row) structure, which include all the void space in black (left side images), the void connected with the outside for $\phi = 1$ in blue (center images), $\phi = 5$ in yellow (right side images), while the material is in white.

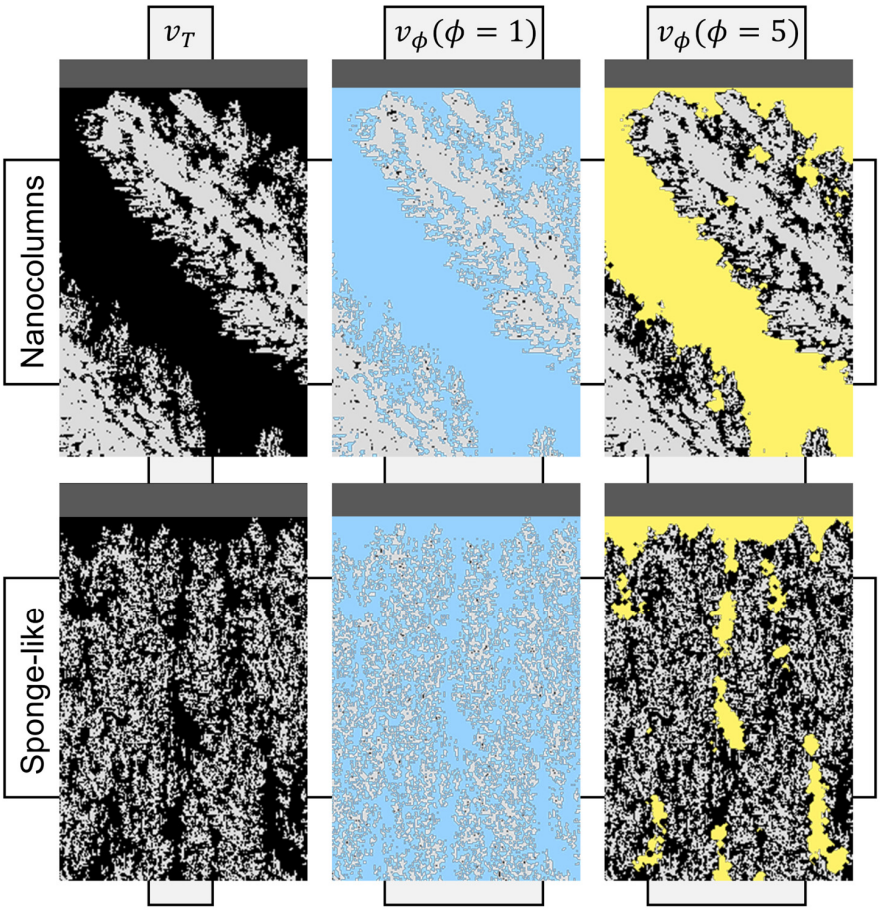

Figure 8. Detailed cross-sectional image of a nanocolumn when $p_g = 0.2$ Pa and $\alpha = 100°$ (**top** row), and of a sponge-like film grown in the high pressure limit (**bottom** row), which include all the void space in black (**left** side images), the volume of the pores connected with the outside for $\phi = 1$ superimposed in blue (**center** images), and $\phi = 5$ superimposed in yellow (**right** side images). The material is in white.

The value of v_ϕ as a function of α has been calculated for a pressure of $p_g = 0.2$ Pa and for $\phi = 1$ and $\phi = 5$, which is displayed in Figure 9a. In this way, when $\phi = 1$ (Figure 9a, top image), the pore throat is so small that the pore connectivity is the highest, so pores connected with the outside penetrate deep into the film, filling almost all the void space (see Figure 8, top row central image). Consequently, $v_{\phi=1}$ follows a similar trend as v_T in Figure 7, since there are very few occluded pores under these conditions. Hence, the four regions mentioned above when discussing Figure 7 are also found now, finding that $v_{\phi=1}$ reaches a maximum value whenever $\alpha > \alpha_M$, i.e., throughout the whole structural transition from a columnar to a sponge-like morphology. On the other hand, when $\phi = 5$, only voids connected by large throats are taken into consideration (see Figure 8, right images). The dependence of $v_{\phi=5}$ with α appears in Figure 9a (bottom image), where the maximum value is achieved when $\alpha = \alpha_M$, i.e., when the nanostructure is clearly nanocolumnar, unlike the $\phi = 1$ case. The origin of this difference resides on the small

size of the voids produced by the incorporation of Brownian-like species when $\alpha > \alpha_M$, which are not accounted when $\phi = 5$ (see Figure 8 top and bottom row). The contact area of the pores has been calculated under the same conditions as in Figure 9a for $\phi = 1$ and $\phi = 5$, and is displayed in Figure 9b. Remarkably, $a_{\phi=1}$ shows the same trend as $v_{\phi=1}$ when $\alpha < \alpha_M$. However, when $\alpha \gtrsim \alpha_M$ the behavior is quite different: now the structural shift from nanocolumnar to sponge-like produces an increasing trend for $a_{\phi=1}$, implying that the pore area is not constant with α in this range, unlike $v_{\phi=1}$. Conversely, the trend depicted by $a_{\phi=5}$ is quite similar to that of $v_{\phi=5}$ in the whole α range, with a clear maximum value when $\alpha = \alpha_M$. Again, similar results are obtained when increasing the film pressure up to 1 Pa (see Figure 9b). In this way, the obtained results regarding the void connectivity can be summarized as follows:

- When the connectivity through micropores ($\phi = 1$) is analyzed, the maximum volume of the voids in contact with the outside is obtained when $\alpha \gtrsim \alpha_M$, i.e., during the whole structural transition from nanocolumnar to sponge-like morphologies. However, its area is only maximum for this second morphology. Consequently, the maximum values of v_ϕ and a_ϕ are achieved when the morphology is formed by vertically aligned sponge-like nanostructures, i.e., when the growth is dominated by Brownian-like species (at high pressures irrespective of the angle or at low pressures when $\alpha \sim 180°$).
- When the connectivity through mesopores ($\phi = 5$) is analyzed, the maximum volume and area of the voids connected with the outside is obtained when the film morphology is nanocolumnar, when $\alpha = \alpha_M$.

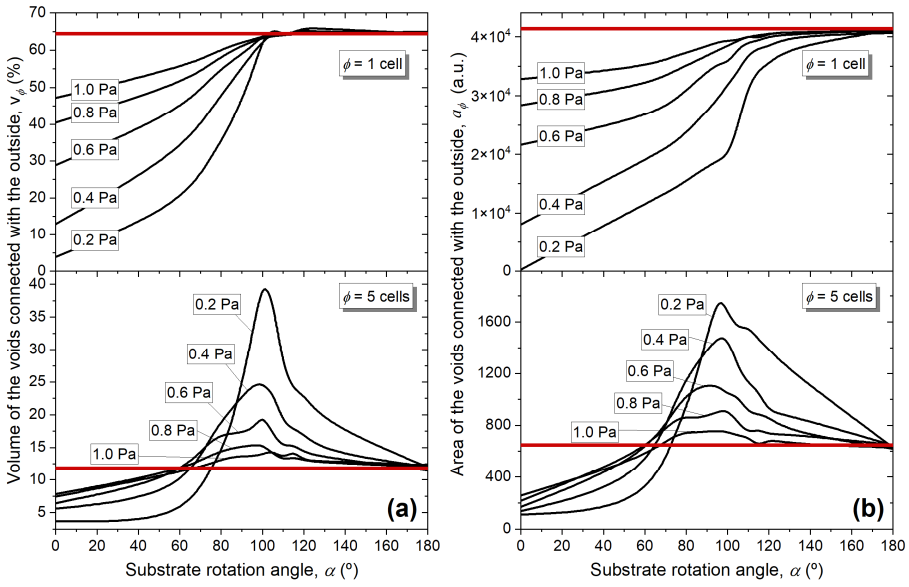

Figure 9. Volume (**a**) and area (**b**) of the pores connected with the outside of the film, for $\phi = 1$ (**top**) and $\phi = 5$ (**bottom**), and for different values of the deposition pressure, p_g, and substrate rotation angle, α. The thick horizontal red lines correspond to the values obtained for the films grown in the high-pressure limit.

This important difference between the two relevant morphologies explains the results in Ref. [3], in which, as mentioned in the introduction, a WO_3 coating was employed as a cathode for electrochromic applications when using a $LiClO_4$ solution in propylene carbonate as electrolyte, and where the performance of columnar and sponge-like morphologies was tested. There, it was determined that the best behavior corresponded to the latter film, i.e., the film that possessed a higher volume and area of the pores connected with the outside by micropores. This same result is expected whenever the performance of the film is related to the penetration of a fluid through the pores, as these could diffuse through micropores (it is important to mention here that there are other important aspects to consider, such as the diffusivity and the typical filling and emptying time of the pores, that may also have an

important impact in the performance of the films). In addition, for other applications that demand larger pore throats, e.g., nanoparticle or large molecule infiltration into the film, it is expected to find an opposite behavior, being the nanocolumnar morphology more adequate than the sponge-like morphology. For instance, in Ref. [59], a nanocolumnar TiO_2 thin film was infiltrated with a dye, while in Ref. [60], Ag and Au nanoparticles were synthesized in a nanocolumnar film by infiltrating it with different solutions.

4. Conclusions

In this article, a well-tested and accurate thin film growth model by MS-OAD has been used to systematically analyze the influence of key experimentally controllable quantities, such as the operating pressure and angle of incidence of the deposition flux, on the morphology and void connectivity of TiO_2 thin films. Overall, three different characteristic morphologies have been obtained when the deposition takes place at low pressures: (i) compact morphology when the rotation angle is below 60°, (ii) a morphology defined by tilted pores that extends from the very surface of the film to the bottom for $60^\circ \lesssim \alpha \lesssim 85^\circ$, and (iii) a morphology characterized by tilted and isolated nanocolumns when $85^\circ \lesssim \alpha \lesssim \alpha_M$, with $\alpha_M \sim 100^\circ$ for a pressure of 0.2 Pa. In addition, a fourth characteristic nanostructure has been obtained when α surpasses the critical value α_M, above which the tilted nanocolumns start to straighten up and become more coalescent and with a sponge-like morphology. In this way, in the limit case $\alpha \sim 180^\circ$, the obtained morphology resembled that of a film grown at relatively high pressures, which contains vertically aligned and coalescent porous nanostructures. Furthermore, for increasing pressures, the same four characteristic nanostructures are found, although the particular value of α_M shifted towards lower values. In the limit case of very high pressures, only this latter structure is found no matter the value of α. Moreover, the appearance of these characteristic morphologies has been analyzed in terms of the transport of sputtered species in the plasma gas and the existence of ballistic and Brownian-like deposition species in the reactor.

The connectivity of the voids inside these films with the outside has also been studied, either by micropores with a pore throat of 0.4 nm, or by mesopores with a pore throat of 2 nm. In this way, it is found that attending to the connectivity by micropores, the morphology that optimizes the volume and area of the voids connected with the outside corresponds to films formed by vertically aligned sponge-like coalescent structures, typically grown at relatively high pressures. However, if the connectivity is analyzed in terms of mesopores, the best conditions to optimize the volume and area of these voids are those of a nanocolumnar thin film, typically grown by MS-OAD at low pressures. The implications of the obtained results have been discussed in terms of the potential applications of these films.

Supplementary Materials: The following supporting information can be downloaded at: https://www.mdpi.com/article/10.3390/coatings13060991/s1, Figure S1. Differential void space as a function of the substrate rotation angle and for different values of the gas pressure.

Author Contributions: Software, R.A.; Formal analysis, G.A.; Investigation, R.A., G.R., H.A.-R., V.R. and A.P.; Writing—original draft, A.P.; Writing—review & editing, A.R.G.-E.; Supervision, A.P.; Funding acquisition, A.P. All authors have read and agreed to the published version of the manuscript.

Funding: The authors acknowledge projects PID2020-114270RA-I00, PID2021-126524NB-I00, PID2021-123879OB-C21, and PID2020-112620GB-I00 funded by MCIN/AEI/10.13039/501100011033; project TED2021-130124A-I00 funded by MCIN/AEI/10.13039/501100011033 and the European Union NextGeneration EU/PRTR; projects US-1380977 and US-1381045 funded by Fondo Europeo de Desarrollo Regional (FEDER) and Consejería de Transformación Económica, Industria, Conocimiento y Universidades de la Junta de Andalucía, within Programa Operativo FEDER 2014–2020; project P18-RT-3480 funded by Consejería de Economía, Conocimiento, Empresas y Universidad de la Junta de Andalucía (PAIDI-2020), the H2020-EU.1.2.1-FET OPEN program (Grant No. 899352, project SOUNDofICE, and the EFRE Infra-Pro project ChAMP); and the University of Seville (VI PPIT-US). Guillermo Regodón would like to acknowledge funding from the European Comission-NextGenerationEU through the "Plan de Recuperación, Transformación y Resiliencia" from the Spanish Government.

Institutional Review Board Statement: Not applicable.

Informed Consent Statement: Not applicable.

Data Availability Statement: Not applicable.

Conflicts of Interest: The authors declare no conflict of interest.

References

1. Barranco, A.; Borras, A.; Gonzalez-Elipe, A.R.; Palmero, A. Perspectives on oblique angle deposition of thin films: From fundamentals to devices. *Prog. Mater. Sci.* **2016**, *76*, 59–153. [CrossRef]
2. He, Y.; Fu, J.; Zhao, Y. Oblique angle deposition and its applications in plasmonics. *Front. Phys.* **2014**, *9*, 47–59. [CrossRef]
3. Louloudakis, D.; Mouratis, K.; Gil-Rostra, J.; Koudoumas, E.; Alvarez, R.; Palmero, A.; Gonzalez-Elipe, A.R. Electrochromic response and porous structure of WO3 cathode layers. *Electrochim. Acta* **2021**, *376*, 138049. [CrossRef]
4. Chundak, M.; Khalakhan, I.; Kúš, P.; Duchoň, T.; Potin, V.; Cacucci, A.; Tsud, N.; Matolín, V.; Veltruská, K. Tailoring of highly porous SnO_2 and SnO_2-Pd thin films. *Mater. Chem. Phys.* **2019**, *232*, 485–492. [CrossRef]
5. Lintymer, J.; Martin, N.; Chappé, J.-M.; Delobelle, P.; Takadoum, J. Nanoindentation of chromium zigzag thin films sputter deposited. *Surf. Coat. Technol.* **2005**, *200*, 269–272. [CrossRef]
6. Boukhalfa, H.; Potin, V.; Martin, N. Structural and electrical properties of nanocolumnar W-Mo thin films with a Janus-like structure. *Surf. Coat. Technol.* **2022**, *448*, 128928. [CrossRef]
7. Garcia-Garcia, F.; Gil-Rostra, J.; Terriza, A.; González, J.; Cotrino, J.; Frutos, F.; Ferrer, F.; González-Elipe, A.; Yubero, F. Low refractive index SiOF thin films prepared by reactive magnetron sputtering. *Thin Solid Films* **2013**, *542*, 332–337. [CrossRef]
8. Maudet, F.; Lacroix, B.; Santos, A.J.; Paumier, F.; Paraillous, M.; Hurand, S.; Corvisier, A.; Marsal, C.; Giroire, B.; Dupeyrat, C.; et al. Optical and nanostructural insights of oblique angle deposited layers applied for photonic coatings. *Appl. Surf. Sci.* **2020**, *520*, 146312. [CrossRef]
9. Büttner, A.; Probst, A.-C.; Emmerich, F.; Damm, C.; Rellinghaus, B.; Döhring, T.; Stollenwerk, M. Influence of sputtering pressure on microstructure and layer properties of iridium thin films. *Thin Solid Films* **2018**, *662*, 41–46. [CrossRef]
10. Vitrey, A.; Alvarez, R.; Palmero, A.; González, M.U.; García-Martín, J.M. Fabrication of black-gold coatings by glancing angle deposition with sputtering. *Beilstein J. Nanotechnol.* **2017**, *8*, 434–439. [CrossRef]
11. Shahidi, M.; Dizaji, H.R.; Ehsani, M.; Ghazi, M. Effect of GLAD technique on optical and electrical properties of $SnO_2/Ag/SnO_2$ structure. *Infrared Phys. Technol.* **2020**, *106*, 103263. [CrossRef]
12. Navarro, E.; González, M.U.; Béron, F.; Tejo, F.; Escrig, J.; García-Martín, J.M. Large-Area Nanopillar Arrays by Glancing Angle Deposition with Tailored Magnetic Properties. *Nanomaterials* **2022**, *12*, 1186. [CrossRef]
13. Rodrigues, M.S.; Borges, J.; Proença, M.; Pedrosa, P.; Martin, N.; Romanyuk, K.; Kholkin, A.L.; Vaz, F. Nanoplasmonic response of porous Au-TiO_2 thin films prepared by oblique angle deposition. *Nanotechnology* **2019**, *30*, 225701. [CrossRef]
14. Martín, M.; Salazar, P.; Álvarez, R.; Palmero, A.; López-Santos, C.; González-Mora, J.; González-Elipe, A.R. Cholesterol biosensing with a polydopamine-modified nanostructured platinum electrode prepared by oblique angle physical vacuum deposition. *Sens. Actuators B Chem.* **2017**, *240*, 37–45. [CrossRef]
15. Ollitrault, J.; Martin, N.; Rauch, J.-Y.; Sanchez, J.-B.; Berger, F. Improvement of ozone detection with GLAD WO3 films. *Mater. Lett.* **2015**, *155*, 1–3. [CrossRef]
16. Sengstock, C.; Lopian, M.; Motemani, Y.; Borgmann, A.; Khare, C.; Buenconsejo, P.J.; Schildhauer, T.; Ludwig, A.; Köller, M. Structure-related antibacterial activity of a titanium nanostructured surface fabricated by glancing angle sputter deposition. *Nanotechnology* **2014**, *25*, 195101. [CrossRef]
17. Yoo, Y.J.; Lim, J.H.; Lee, G.J.; Jang, K.-I.; Song, Y.M. Ultra-thin films with highly absorbent porous media fine-tunable for coloration and enhanced color purity. *Nanoscale* **2016**, *9*, 2986–2991. [CrossRef]
18. Liu, Y.; Zhao, Y.; Feng, Y.; Shen, J.; Liang, X.; Huang, J.; Min, J.; Wang, L.; Shi, W. The influence of incident angle on physical properties of a novel back contact prepared by oblique angle deposition. *Appl. Surf. Sci.* **2016**, *363*, 252–258. [CrossRef]
19. Polat, B.; Keles, O. The effect of copper coating on nanocolumnar silicon anodes for lithium ion batteries. *Thin Solid Films* **2015**, *589*, 543–550. [CrossRef]
20. Lee, Y.-J.; Yang, Z.-P.; Lo, F.-Y.; Siao, J.-J.; Xie, Z.-H.; Chuang, Y.-L.; Lin, T.-Y.; Sheu, J.-K. Slanted n-ZnO/p-GaN nanorod arrays light-emitting diodes grown by oblique-angle deposition. *APL Mater.* **2014**, *2*, 056101. [CrossRef]
21. Singh, A.; Sharma, A.; Tomar, M.; Gupta, V. Growth of highly porous ZnO nanostructures for carbon monoxide gas sensing. *Surf. Coat. Technol.* **2018**, *343*, 49–56. [CrossRef]
22. Gil-Rostra, J.; García-García, F.; Yubero, F.; González-Elipe, A.R. Tuning the transmittance and the electrochromic behavior of CoxSiyOz thin films prepared by magnetron sputtering at glancing angle. *Sol. Energy Mater. Sol. Cells* **2014**, *123*, 130–138. [CrossRef]
23. Borhani-Haghighi, S.; Khare, C.; Trócoli, R.; Dushina, A.; Kieschnick, M.; LaMantia, F.; Ludwig, A. Synthesis of nanostructured $LiMn_2O_4$thin films by glancing angle deposition for Li-ion battery applications. *Nanotechnology* **2016**, *27*, 455402. [CrossRef]

24. Limwichean, S.; Kasayapanand, N.; Ponchio, C.; Nakajima, H.; Patthanasettakul, V.; Eiamchai, P.; Meng, G.; Horprathum, M. Morphology-controlled fabrication of nanostructured WO3 thin films by magnetron sputtering with glancing angle deposition for enhanced efficiency photo-electrochemical water splitting. *Ceram. Int.* **2021**, *47*, 34455–34462. [CrossRef]
25. El Mohajir, A.; Pour Yazdi, M.A.; Krystianiak, A.; Heintz, O.; Martin, N.; Berger, F.; Sanchez, J.-B. Nanostructuring of SnO_2 Thin Films by Associating Glancing Angle Deposition and Sputtering Pressure for Gas Sensing Applications. *Chemosensors* **2022**, *10*, 426. [CrossRef]
26. Barbillon, G.; Humbert, C.; González, M.U.; García-Martín, J.M. Gold Nanocolumnar Templates for Effective Chemical Sensing by Surface-Enhanced Raman Scattering. *Nanomaterials* **2022**, *12*, 4157. [CrossRef]
27. Alvarez, R.; Muñoz-Piña, S.; González, M.U.; Izquierdo-Barba, I.; Fernández-Martínez, I.; Rico, V.; Arcos, D.; García-Valenzuela, A.; Palmero, A.; Vallet-Regi, M.; et al. Antibacterial Nanostructured Ti Coatings by Magnetron Sputtering: From Laboratory Scales to Industrial Reactors. *Nanomaterials* **2019**, *9*, 1217. [CrossRef]
28. Mobini, S.; González, M.U.; Caballero-Calero, O.; Patrick, E.E.; Martín-González, M.; García-Martín, J.M. Effects of nanostructuration on the electrochemical performance of metallic bioelectrodes. *Nanoscale* **2022**, *14*, 3179–3190. [CrossRef]
29. Godinho, V.; Moskovkin, P.; Álvarez, R.; Caballero-Hernández, J.; Schierholz, R.; Bera, B.; Demarche, J.; Palmero, A.; Fernández, A.; Lucas, S. On the formation of the porous structure in nanostructured a-Si coatings deposited by dc magnetron sputtering at oblique angles. *Nanotechnology* **2014**, *25*, 355705. [CrossRef]
30. García-Valenzuela, A.; Butterling, M.; Liedke, M.O.; Hirschmann, E.; Trinh, T.T.; Attallah, A.G.; Wagner, A.; Alvarez, R.; Gil-Rostra, J.; Rico, V.J.; et al. Positron annihilation analysis of nanopores and growth mechanism of oblique angle evaporated TiO_2 and SiO_2 thin films and multilayers. *Microporous Mesoporous Mater.* **2019**, *295*, 109968. [CrossRef]
31. González-García, L.; Parra-Barranco, J.; Sánchez-Valencia, J.R.; Barranco, A.; Borrás, A.; González-Elipe, A.R.; García-Gutiérrez, M.-C.; Hernández, J.J.; Rueda, D.R.; Ezquerra, T.A. Correlation lengths, porosity and water adsorption in TiO_2thin films prepared by glancing angle deposition. *Nanotechnology* **2012**, *23*, 205701. [CrossRef]
32. Krause, K.M.; Thommes, M.; Brett, M.J. Pore analysis of obliquely deposited nanostructures by krypton gas adsorption at 87K. *Microporous Mesoporous Mater.* **2011**, *143*, 166–173. [CrossRef]
33. Muñoz-Piña, S.; Garcia-Valenzuela, A.; Oyarzabal, E.; Gil-Rostra, J.; Rico, V.; Alcalá, G.; Alvarez, R.; Tabares, F.; Palmero, A.; Gonzalez-Elipe, A. Wetting and spreading of liquid lithium onto nanocolumnar tungsten coatings tailored through the topography of stainless steel substrates. *Nucl. Fusion* **2020**, *60*, 126033. [CrossRef]
34. Hawkeye, M.M.; Taschuk, M.T.; Brett, M.J. *Glancing Angle Deposition of Thin Films: Engineering the Nanoscale*; Wiley Series in Materials for Electronic & Optoelectronic Applications; John Wiley & Sons: New York, NY, USA, 2014; ISBN 978-1-118-84756.
35. Pelliccione, M.; Lu, T.-M. *Evolution of Thin Film Morphology: Modeling and Simulations*; Springer Series Materials Science; Springer: Berlin/Heidelberg, Germany, 2008; Volume 108, ISBN 978-0-387-75108-5.
36. Vári, G.; Óvári, L.; Kiss, J.; Kónya, Z. LEIS and XPS investigation into the growth of cerium and cerium dioxide on Cu(111). *Phys. Chem. Chem. Phys.* **2015**, *17*, 5124–5132. [CrossRef]
37. Óvári, L.; Bugyi, L.; Majzik, Z.; Berkó, A.; Kiss, J. Surface Structure and Composition of Au−Rh Bimetallic Nanoclusters on TiO_2(110): A LEIS and STM Study. *J. Phys. Chem. C* **2008**, *112*, 18011–18016. [CrossRef]
38. Lopez-Santos, C.; Alvarez, R.; Garcia-Valenzuela, A.; Rico, V.; Loeffler, M.; Gonzalez-Elipe, A.R.; Palmero, A. Nanocolumnar association and domain formation in porous thin films grown by evaporation at oblique angles. *Nanotechnology* **2016**, *27*, 395702. [CrossRef]
39. Depla, D.; Mahieu, S. (Eds.) *Reactive Sputter Deposition*; Springer Series in Materials Science; Springer: Berlin/Heidelberg, Germany, 2008; Volume 109, ISBN 978-3-540-76662-9.
40. Depla, D. (Ed.) *Magnetrons, Reactive Gases and Sputtering*; Diederik Depla: Ghent, Belgium, 2020; ISBN 978-1-304-34781-7.
41. Garcia-Valenzuela, A.; Alvarez, R.; Rico, V.; Cotrino, J.; Gonzalez-Elipe, A.; Palmero, A. Growth of nanocolumnar porous TiO_2 thin films by magnetron sputtering using particle collimators. *Surf. Coat. Technol.* **2018**, *343*, 172–177. [CrossRef]
42. Alvarez, R.; García-Martín, J.M.; Macías-Montero, M.; Gonzalez-Garcia, L.; González, J.C.; Rico, V.; Perlich, J.; Cotrino, J.; González-Elipe, A.R.; Palmero, A. Growth regimes of porous gold thin films deposited by magnetron sputtering at oblique incidence: From compact to columnar microstructures. *Nanotechnology* **2013**, *24*, 045604. [CrossRef]
43. Alvarez, R.P.; Romero-Gomez, J.; Gil-Rostra, J.; Cotrino, F.; Yubero, A.; Palmero, A.R.; Gonzalez-Elipe, J. Influence of plasma-generated negative oxygen ion impingement on magnetron sputtered amorphous SiO_2 thin films during growth at low temperatures. *J. Appl. Phys.* **2010**, *108*, 064316. [CrossRef]
44. Alvarez, R.; Garcia-Martin, J.M.; Lopez-Santos, M.C.; Rico, V.; Ferrer, F.J.; Cotrino, J.; Gonzalez-Elipe, A.R.; Palmero, A. On the Deposition Rates of Magnetron Sputtered Thin Films at Oblique Angles. *Plasma Process. Polym.* **2014**, *11*, 571–576. [CrossRef]
45. Lowell, S.; Shields, J.E.; Thomas, M.A. *Characterization of Porous Solids and Powders: Surface Area, Pore Size and Density*; Springer: Berlin/Heidelberg, Germany, 2006; pp. 212–232. ISBN 978-1-4020-2303-3.
46. García-Valenzuela, A.; Alvarez, R.; Espinós, J.P.; Rico, V.; Gil-Rostra, J.; Palmero, A.; Gonzalez-Elipe, A.R. SiOx by magnetron sputtered revisited: Tailoring the photonic properties of multilayers. *Appl. Surf. Sci.* **2019**, *488*, 791–800. [CrossRef]
47. Oliva-Ramirez, M.; Barranco, A.; Löffler, M.; Yubero, F.; González-Elipe, A.R. Optofluidic Modulation of Self-Associated Nanostructural Units Forming Planar Bragg Microcavities. *ACS Nano* **2016**, *10*, 1256–1264. [CrossRef] [PubMed]

48. Alvarez, R.; Garcia-Valenzuela, A.; Regodon, G.; Ferrer, F.J.; Rico, V.; Garcia-Martin, J.M.; Gonzalez-Elipe, A.R.; Palmero, A. Hyperthermal Relaxation Schemes in Nanocolumnar Thin Films Grown by Magnetron Sputtering at Oblique Angles. *Surf. Coat. Technol.* 2023, *in progress*.
49. SRIM 2013. Available online: www.srim.org/ (accessed on 22 May 2023).
50. Van Aeken, K. SIMTRA. Available online: www.draft.ugent.be/ (accessed on 22 May 2023).
51. Van Aeken, K.; Mahieu, S.; Depla, D. The metal flux from a rotating cylindrical magnetron: A Monte Carlo simulation. *J. Phys. D Appl. Phys.* **2008**, *41*, 20530. [CrossRef]
52. Alvarez, R.; Garcia-Martin, J.M.; Garcia-Valenzuela, A.; Macias-Montero, M.; Ferrer, F.J.; Santiso, J.; Rico, V.; Cotrino, J.; Gonzalez-Elipe, A.R.; Palmero, A. Nanostructured Ti thin films by magnetron sputtering at oblique angles. *J. Phys. D Appl. Phys.* **2016**, *49*, 045303. [CrossRef]
53. Thornton, J.A. Influence of apparatus geometry and deposition conditions on the structure and topography of thick sputtered coatings. *J. Vac. Sci. Technol.* **1974**, *11*, 666–670. [CrossRef]
54. Thornton, J.A. Influence of substrate temperature and deposition rate on structure of thick sputtered Cu coatings. *J. Vac. Sci. Technol.* **1975**, *12*, 830–835. [CrossRef]
55. Alvarez, R.; Lopez-Santos, C.; Ferrer, F.J.; Rico, V.; Cotrino, J.; Gonzalez-Elipe, A.R.; Palmero, A. Modulating Low Energy Ion Plasma Fluxes for the Growth of Nanoporous Thin Films. *Plasma Process. Polym.* **2015**, *12*, 719–724. [CrossRef]
56. Alvarez, R.; Garcia-Valenzuela, A.; Lopez-Santos, C.; Ferrer, F.J.; Rico, V.; Guillen, E.; Alcon-Camas, M.; Escobar-Galindo, R.; Gonzalez-Elipe, A.R.; Palmero, A. High-Rate Deposition of Stoichiometric Compounds by Reactive Magnetron Sputtering at Oblique Angles. *Plasma Process. Polym.* **2016**, *13*, 960–964. [CrossRef]
57. Alvarez, R.; Romero-Gomez, P.; Gil-Rostra, J.; Cotrino, J.; Yubero, F.; Gonzalez-Elipe, A.R.; Palmero, A. Growth of SiO_2 and TiO_2 thin films deposited by reactive magnetron sputtering and PECVD by the incorporation of non-directional deposition fluxes. *Phys. Status Solidi A* **2013**, *210*, 796–801. [CrossRef]
58. IUPAC. *Compendium of Chemical Terminology, (The "Gold Book")*, 2nd ed.; McNaught, A.D., Wilkinson, A., Eds.; Blackwell Scientific Publications: Oxford, UK, 1997; ISBN 0-9678550-9-8. [CrossRef]
59. Rico, V.J.; Turk, H.; Yubero, F.; Gonzalez-Elipe, A.R. Titania Enhanced Photocatalysis and Dye Giant Absorption in Nanoporous 1D Bragg Microcavities. *ACS Appl. Nano Mater.* **2022**, *5*, 5487–5497. [CrossRef] [PubMed]
60. Parra-Barranco, J.; Sanchez-Valencia, J.R.; Barranco, A.; González-Elipe, A.R. Silver and gold nanoparticles in nanometric confined templates: Synthesis and alloying within the anisotropic pores of oblique angle deposited films. *Nanotechnology* **2017**, *28*, 485602. [CrossRef] [PubMed]